A study of the silicate emission features of the IRAS low resolution spectra

Gal, O.; Jourdain de Muizon, M.; Papoular, R.; Pegourie, B.

Astron. Astrophys. 183, 29–37 (1987)

ASTRONOMY AND ASTROPHYSICS

A study of the silicate emission features of the IRAS low resolution spectra

O. Gal[1], M. de Muizon[2,3], R. Papoular[4], and B. Pégourie[4]

[1] Ecole Polytechnique, P.M.I., Palaiseau, France
[2] Sterrewacht Leiden, Postbus 9513, NL-23000 RA Leiden, The Netherlands
[3] Observatoire de Paris, Section de Meudon, F-92195 Meudon Principal Cedex, France
[4] Service d'Astrophysique, CEN Saclay, Service d'Astrophysique, F-91191 Gif-sur-Yvette Cédex, France

Received February 3, 1986; accepted February 4, 1987

Summary. Using the IRAS catalog of low resolution spectra, we have analyzed 1808 silicate emission features, the union of classes 2*n* and 6*n*. The sample size is large enough to establish average properties (e.g. energy distributions); correlations between luminosities, excesses, colour and coordinates; histograms and galactic distributions, with a good degree of confidence. Of particular interest are: the detection of the largest silicate excesses ever observed ($\gtrsim 10$) and their being located in the bulge of the Galaxy; the progressive strengthening of the 10-μm silicate feature as the objects become fainter (and hence more distant); the tendency for the 10-μm excess to decrease as the galactic latitude increases; the ranges of "effective" dust temperatures (150 to 500 K), star colour temperatures (700 to 5000 K) and envelope optical thicknesses (0 to ~ 0.5 at 10 μm). This analysis also points to the similarity of dust properties between IRAS objects and previously observed Long Period Variables.

Key words: stellar content of galaxies – infrared radiation – interstellar medium: dust, extinction – stars: circum. stellar matter – late-type stars

1. Introduction

The Dutch Low-Resolution Spectrometer (LRS) aboard the IRAS satellite (Wildeman et al., 1983) recorded a large number of spectra in the spectral bands 7.5–13.5 and 11–23 μm, with a resolution varying from ~ 15 at the blue end to ~ 40 at the red end of each band. These spectra have been classified in 10 classes according to their characteristic features (Beichman et al., 1985) and Olnon (1985) made their first statistical analysis.

Because the IRAS mission was in the nature of a survey, only a fraction of the spectra have a high signal-to-noise ratio. However, thanks to the large number of spectra in most classes, suitable statistical procedures make it possible to extract very useful information about the common properties of spectra in each class, and compare different classes.

Send offprint requests to: R. Papoular

Also, the sensitivity of the survey allows us to probe deep into the Galaxy and study the distribution of various stellar types relative to the galactic arms.

We have studied all the classes of spectra, along with the corresponding survey photometry in the 4 bands: 12, 25, 60 and 100 μm. Here, however, we concentrate on the 8–22 μm range and on the spectra which exhibit conspicuous silicate dust features at ~ 10 and ~ 20 μm: 1730 in class 2 and 78 in class 6. We found no such spectra in the other classes, except for only 7 among the 363 "unidentified spectra" (class 0). Since the corresponding sources are not extended, they are assumed to be evolved stars with circumstellar (CS) shells.

The total set of interest comprises 1808 objects ($\sim 40\%$ of the LRS Catalog). This range is large enough that one can subdivide it in subclasses and still have good statistics. In Sect. 2, we obtain good-quality average spectra which significantly improve our knowledge of the 20-μm silicate band, as compared to data from earth-bound observatories. It also becomes possible to distinguish clear trends in the evolution of spectral profiles and feature strengths from bright to faint objects.

In Sect. 3, we extract the IR excess from 8 to 22 μm and study in more detail its colours and intensities. From these, we estimate the ranges of temperatures and thicknesses spanned by the dust shells as well as the range of photospheric temperatures. Striking correlations emerge between the last two quantities and the brightnesses, which hint at a distance dependence. This leads us, in Sect. 4, to study the galactic distribution of the CS shells and of their physical properties. Again, clear correlations are found between the latter and the galactic coordinates. Finally, in Sect. 5, we use a more sophisticated radiative transfer modeling to analyze the properties of two particular groups of shells.

2. Average spectra

A quick perusal of the spectra of interest shows that they differ considerably from one another, although both the 10- and 18-μm features are clearly recognizable on most of them. The differences bear on the intensity of the features, their width and the general slope of the spectrum ("blue" and "red" spectra) as well as the brightness at 8 μm. Since the 2 peaks are practically always located at the same wavelengths, these differences are probably due to variations in the size, density and temperature of the CS

envelopes, the size and physical state of the dust grains and, of course, the size, temperature and distance of the central star, rather than to variations in the dust chemical composition. It is therefore sensible to treat all objects of classes $2n$ and $6n$ together but, at the same time, it is necessary to sort them out into relatively homogeneous subclasses. It appears that the most effective single discriminant for this purpose is the brightness (at 8 μm, for instance). Since the latter must be binned in finite intervals, a suitable averaging has still to be performed over the objects in each of the corresponding subclasses. We adopted the following procedure. First normalize the flux densities, $F_j(\lambda_i)$, of a given subclass to the flux density at some convenient λ_0 (here, $\sim 8\,\mu$m), since we are mainly interested in spectral profiles. Then compute the *geometric* average of the normalized spectra, $\mathscr{F}_j(\lambda_i)$, of a given group of N objects, λ by λ:

$$\overline{\mathscr{F}}(\lambda_i) = \left(\prod_{j=1}^{N} \mathscr{F}_j(\lambda_i) \right)^{1/N}, \tag{1}$$

which is equivalent to taking the exponential of the average of $\ln \mathscr{F}_j(\lambda_i)$, which has the advantage of reducing the bias towards larger relative fluxes, but also the disadvantage of not being applicable in case of a strong negative spike driving F_i below the base line. In such a case, we simply ignore the negative F_i value and if this happens at the reference wavelength, λ_0, we skip the object altogether; the frequency of such events is quite small because extremely noisy spectra have not been included in the catalog.

To asses the degree of significance of the average normalized spectrum, $\overline{\mathscr{F}}$, we also compute a sample (geometric) standard deviation, $\sum_{\mathscr{F}}(\lambda_i)$, defined as the exponential of the corresponding standard deviation of $\ln \mathscr{F}_j(\lambda_i)$. For identical spectra, $\sum_{\mathscr{F}} = 1$. In cases where the noise component is small, or can be accounted for, $\sum_{\mathscr{F}}$ gives a measure of the dispersion of the overall spectral profile of the objects in the subclass under consideration.

We characterize the noise component by the standard deviation, $\sigma_{D_2}(\lambda_i)$, of the quantity

$$D_2(\lambda_i) = [F(\lambda_{i+2})/F(\lambda_{i+1})]/[F(\lambda_{i+1})/F(\lambda_i)]$$
$$= F(\lambda_{i+2})F(\lambda_i)/F^2(\lambda_{i+1}) \tag{2}$$

This is a sensitive indicator of the "roughness" of a curve since it is directly related to the curvature:

$$D_2(\lambda_i) \simeq 1 + [(d^2F/d\lambda^2)\Delta^2/F]_{\lambda_i},$$

where $\Delta = \lambda_{i+1} - \lambda_i$. Now it can easily be shown that the standard deviations of random fluctuations of $F(\lambda_i)$ and $D_2(\lambda_i)$ are related by

$$\sigma_{D_2} \simeq (\sigma_{D_2})/D_2 = \sqrt{6}\,\frac{\sigma_F}{F} \tag{3}$$

so that $\sigma_{D2}(\lambda_i)$ is a measure of the relative intensity of the noise in $F(\lambda_i)$.

Figure 1 represents $\overline{\mathscr{F}}$ for class 6 (69 objects) and three subclasses of class 2 defined by limits constraining F_{12}, the flux density at 12 μm as measured by the IRAS photometers: a) 0–17.5 Jy (427 objects); b) 25 to 45 Jy (431 objects) and c) above 60 Jy (421 objects).

It can be observed that:

a) As the brightness decreases, the spectra become steadily redder and noisier (especially at the longer wavelengths);

b) The features become steadily stronger (although part of the very largest excesses are artefacts due to noise, as discussed in Sect. 3)

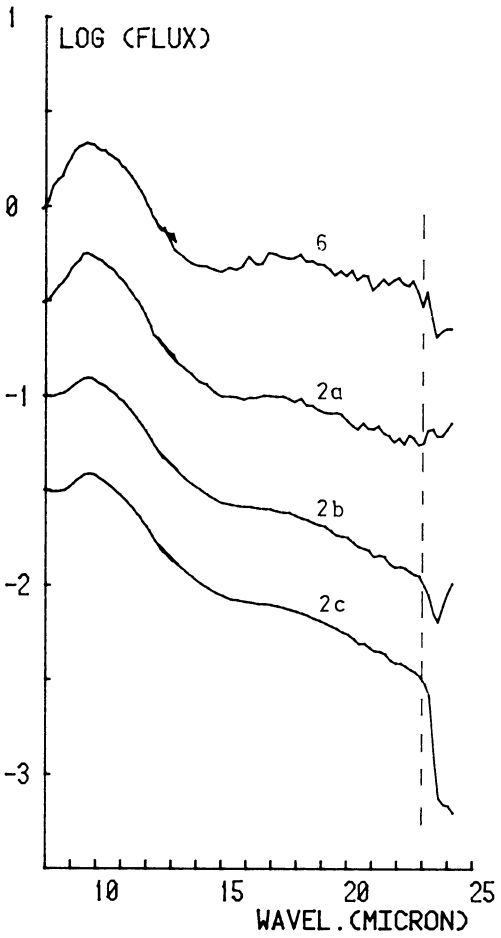

Fig. 1. Average energy distribution (Eq. 1) normalized to 1 at 8 μm for: 69 objects of class 6n; 427 objects of class 2n (subclass 2a), $0 \leq F_{12} < 17.5$ Jy; 431 objects of class 2n (subclass 2b), $25 \leq F_{12} < 45$ Jy; 421 objects of class 2n, with $F_{12} \geq 60$ Jy (subclass 2c). Arbitrary vertical displacement: 0; −0.5; −1; −1.5

c) If the luminosity distribution of the objects is not very sensitive to their location in the Galaxy, then, fainter objects are likely to be also more distant and preferentially more luminous in the mid-IR;

d) The average spectrum of class 6 is quite similar to that of subclass 2a, except that it is globally redder.

Figure 2 represents the dispersions corresponding to the averages of Fig. 1. Again, the curve for class 6 is similar to that of subclass 2a. The noise, as measured by σ_{D2}, increases regularly from subclass 2c to class 6, through subclasses 2b and 2a, and is much larger in the band 11 to 23 μm. This is reflected by the increasing strength of the discontinuity in $\sum_{\mathscr{F}}$ at the reference w.l. ($\sim 8\,\mu$m). For subclass 2c, σ_{D2} never exceeds 6% (hence $\sigma_F/F \lesssim 2.5\%$) between 8 and 12 μm, so that $\sum_{\mathscr{F}}$ is mainly due to variations of global shape and general slope of spectrum from object to object (trends a and b above).

No trace of the SiC feature at 11.5 μm or the H_2O feature at 12 μm or the hydrocarbon feature at 11.3 μm is apparent on the average spectrum of the "good-quality" subclass 2c. More generally, its very smooth profile indicates an amorphous dust material.

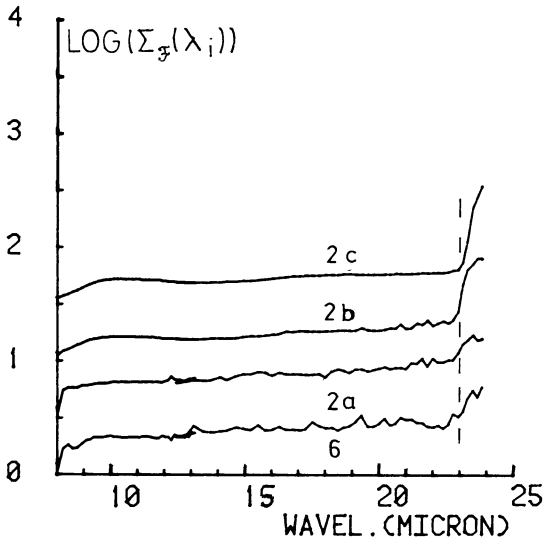

Fig. 2. Spectral dispersions, $\sum_{\mathcal{F}}(\lambda_i)$, corresponding to the samples in Fig. 1. Arbitrary vertical displacement: 0; 0.5; 1; 1.5. The curves in Figs. 1 and 2 are not meaningful beyond $\sim 23\,\mu$m

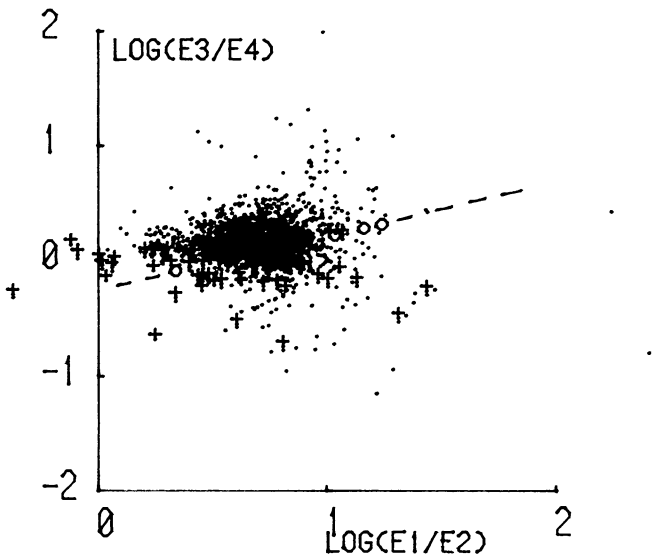

Fig. 3. Colour-colour diagram: the E's are the excesses (Eq. 3) for 10, 19, 14.5 and 22 μm. The dashed line represents a model described in the text, with circles at 200, 400, 500 and 600 K. The crosses represent the objects belonging to class 6*n*, while dots are for class 2*n*; 1753 objects in all

The average spectrum of subclass 2c is very similar to ground-based spectra of Miras (Forrest et al., 1975; 1979); this is further discussed in Sect. 5 and Fig. 10.

3. The infrared excess

The photospheric temperature of the central star, for the objects considered here, is expected to lie between 2000 and 5000 K. For an assumed typical temperature of 3000 K, the photospheric spectrum would be of the form $F_\lambda \propto \lambda^{-3.5}$. Assuming also the IR excess to be negligible at $\lambda_0 = 8\,\mu$m, we can define a lower limit to the IR excess at longer wavelengths, for each object:

$$E_\lambda = F_\lambda - F_{\lambda_0}(\lambda_0/\lambda)^{3.5} \tag{4}$$

Let us consider 4 characteristic wavelengths, $\lambda_1 = 10$, $\lambda_2 = 19$, $\lambda_3 = 14.5$, and $\lambda_4 = 22\,\mu$m, and construct the corresponding excess colours, E_{10}/E_{19} and E_{14}/E_{22} (in fact, in order to reduce the effect of noise, each of the 5 flux densities is taken to be the average of a number of fluxes corresponding to adjacent wavelengths 7.86, 8.04; 9.83, 9.97; 10.11, 10.25; 14.04, 14.32, 14.62, 14.9; 18.89, 19.11, 19.33, 19.55; 21.8, 21.98, 22.17, 22.36 μm). Figure 3 is a colour-colour diagram, drawn with these colours, for the objects of class 2 (dots) and 6 (crosses). Assume now that, as with M-type LPV's, the dust envelopes are optically thin. This is qualitatively borne out by the apparent absence of self-absorption at 10 μm in the overwhelming majority of the IRAS spectra. As a consequence, it is possible to roughly estimate the range of dust temperatures by treating the envelopes as isothermal bodies of temperature T_d and emissivity $\varepsilon_d \propto Q_d$ (grain absorption efficiency). We have used the Q's deduced from a study of ground-based spectra of Miras (Pégourié and Papoular, 1985; Pégourié, 1985): $Q_d(\lambda_1)/a = 1.12$, $Q_d(\lambda_2)/a = 0.37$; $Q_d(\lambda_3)/a = 0.19$; $Q_d(\lambda_4)/a = 0.29$ (for dust grains of radius $a \cong 0.3\,\mu$m). The corresponding colour-colour curve passes through the densest parts of the cloud of points in Fig. 3, which spans a range of temperatures of about 150 to 500 K. Note that, by construction, this is an "effective" envelope temperature, which should be lower than that of the inner CS shell.

Consider now the *relative* excess

$$\mathscr{E}_\lambda = \frac{E_\lambda}{F_{\lambda_0}}\left(\frac{\lambda}{\lambda_0}\right)^{3.5} = \frac{F_\lambda}{F_{\lambda_0}}\left(\frac{\lambda}{\lambda_0}\right)^{3.5} - 1\,. \tag{5}$$

Figure 4 represents the correlation between the $\mathscr{E}_\lambda$'s at the two silicate peaks. Both excesses span a large range and are roughly proportional over this range. This is a confirmation of the common chemical nature of the dust around these objects and of its similarity to the "silicate" dust observed from Earth. Moreover, using a more elaborate model of spherical radiative transfer, it can be shown that the *average* trend of Fig. 4 indicates optical

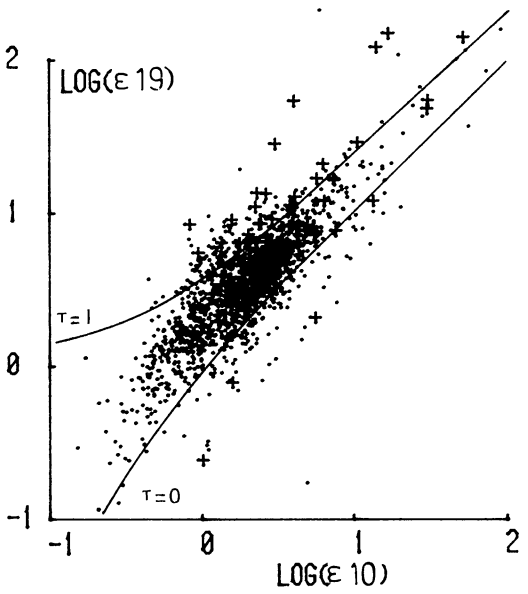

Fig. 4. Correlation between the relative excesses, $\mathscr{E}_{10}$ and $\mathscr{E}_{19}$ at the two silicate peaks, 10 and 19 μm (Eq. 4). Dots for class 2, crosses for class 6; 1783 objects in all. Dashed curves: models for $\tau_{10} = 0$ and 1

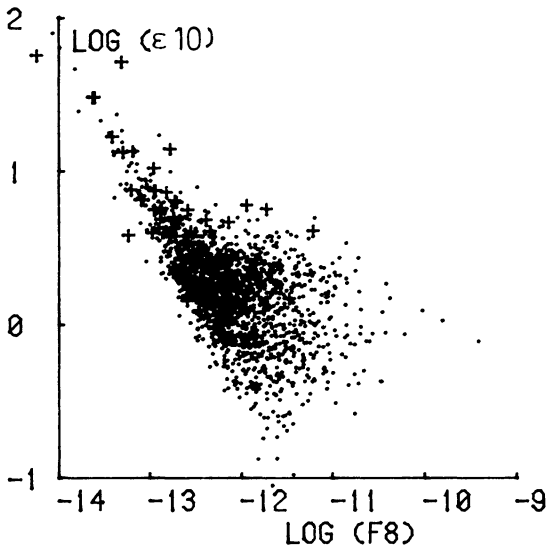

Fig. 5. The 10-μm relative excess as a function of the 8-μm flux density (in $Wm^{-2}\mu^{-1}m$). Dots for class 2, crosses for class 6; 1796 objects in all

thicknesses at 10 μm decreasing from ~ 0.5 to ~ 0 (confirming the assumption of thinness) as $\mathscr{E}_{10}$ varies from 0.1 to 15.

Besides variations of star and envelope parameters, the dispersion of the dots in Figs. 3 and 4 is also due to instrumental noise. In particular, the very large excesses observed in Fig. 4 may be questioned on the ground that they could be artificially produced by the noise which is known to affect low intensity spectra. Figure 5 helps exploring this possibility by showing how $\mathscr{E}_{10}$ correlates with the flux density at 8 μm: F_8 (this is expressed in $Wm^{-2}\mu m^{-1}$, as in the LRS catalog; $F_\lambda(\mathrm{Jy}) = F_\lambda(Wm^{-2}\mu m^{-1})(3.3\,10^{11})\lambda^2(\mu m)$). The largest excesses are indeed associated with the smallest fluxes. Besides, there is a sharp, linear, oblique limit to the cloud of points. Obviously, this is due to a selection effect associated with the classification algorithm devised by Olnon (1985) to build the catalog: a spectrum is classified as $2n$ or $6n$ if $E_{10} > 5\sigma_{10}$ or $\mathscr{E}_{10} > 10\sigma_{10}/F_8$ (since the ratio of continua at 8 and 10 μm is ~ 2). Since the noise level is about $4\,10^{-14}\,Wm^{-2}\mu m^{-1}$, objects with $\mathscr{E}_{10}F_8 \lesssim 4\,10^{-13}$ are eliminated, as observed in Fig. 5. In order to quantitatively interpret the apparent anti-correlation between $\mathscr{E}_{10}$ and F_8, it is therefore necessary to take into account both noise, which spreads out the points along lines of constant $(\mathscr{E}_{10}+1)F_8$, and truncation (by selection), which artificially increases the apparent average excess for a given F_8.

For this purpose, we have subdivided class $2n$ in subgroups corresponding to reasonably populated intervals of F_8 (class $6n$ is too small for this procedure to make sense). For each subgroup, we computed the average excess $\bar{\mathscr{E}}_{10}$ and the standard deviation $\sigma_{\mathscr{E}}$. The former are represented in Fig. 6a by horizontal segments with ordinates $\bar{\mathscr{E}}_{10}$, the latter by dots. Figure 6b represents the number of objects found in small (equal) intervals of $\log F_8$, over the same range of F_8 as Fig. 6a. Beyond $F_8 \sim 5\,10^{-13}$, the slope of this histogram is -1, showing near completeness of the sample in this range, where, moreover, the S/N ratio is $\gtrsim 10$. In this range, therefore, we observe the true $\bar{\mathscr{E}}_{10}$ and $\sigma_{\mathscr{E}}$, the latter being due to a dispersion of the physical properties of the envelopes.

For $F_8 \gtrsim 5\,10^{-13}$, a more quantitative treatment is necessary to assess the significance of the observed values of $\bar{\mathscr{E}}_{10}$ and $\sigma_{\mathscr{E}}$. This is done in the appendix, with the following results.

For $F_8 \gtrsim 10^{-13}$, it is possible to estimate the parameters $\bar{\mathscr{E}}$ σ_t of the parent population (crosses and pentagons in Fig. 6a) that is subjected to instrumental processing. It is found that neither the noise in F_8 nor the selection of the stronger features seriously affect the distributions except, perhaps, at $\sim 1.5\,10^{-13}$:

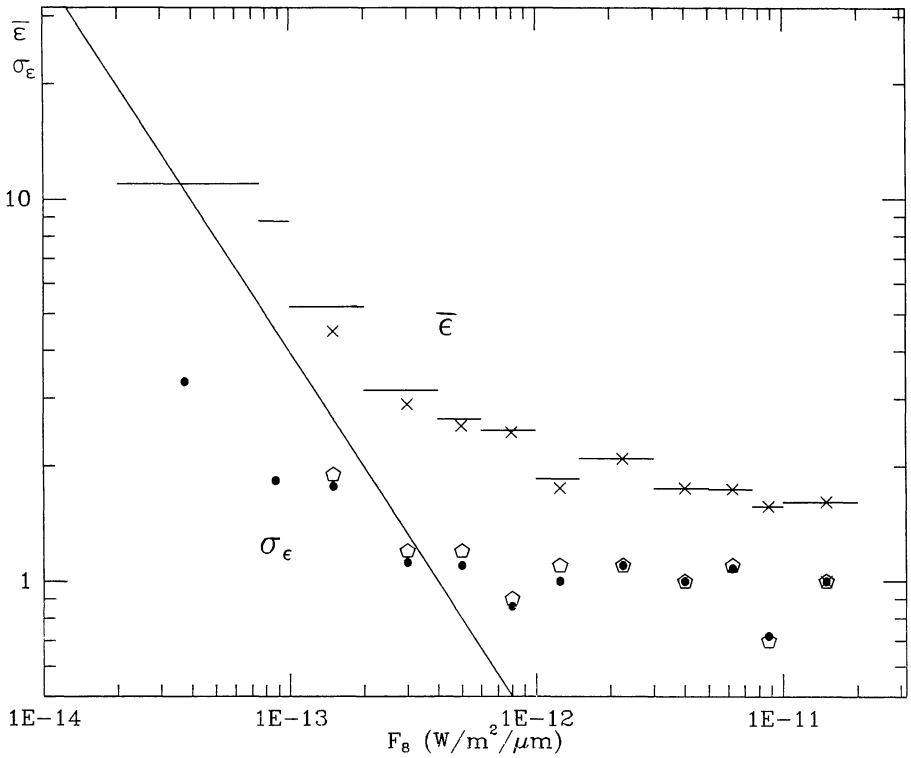

Fig. 6a. The parameters describing the distribution of $\mathscr{E}_{10}$'s for subgroups of class 2: (——) $\bar{\mathscr{E}}_{10}$, the observed average $\mathscr{E}_{10}$; (dots) the observed standard deviation of $\mathscr{E}_{10}$; (crosses) $\mathscr{E}_t$ and (pentagons) σ_t the parameters of the underlying distribution, as estimated in Appendix 1. F_8 is the average of the fluxes at 7.86 and 8.04 μm (in $Wm^{-2}\mu m^{-1}$) for each object. The oblique line represents the selection algorithm, $F_8\mathscr{E}_{10} \geq 4\,10^{-13}$

this is roughly where the slope of the "curve" $\mathscr{E}_{10}$ vs F_8 departs from -1. In this domain, $\mathscr{E}_t$ and σ_t are representative of the true distribution except where another selection effect, if any, is active. If it is indeed the case, as, perhaps, for $F_8 \gtrsim 4\,10^{-13}$ (cf. Fig. 6b), then the observed spectra are not fully representative of the intrinsic population, although not yet biased by noise.

On the other hand, for $F_8 \gtrsim 10^{-13}$, a small number of objects may have immigrated from regions of larger true F_8's and thus increase the apparent "local" average excess (cf. Eq. A2). This effect is entirely due to noise in F_8. Since noises at different λ's are not correlated, it is nonetheless possible to obtain information on this range by reverting to another procedure: average a number of spectra in an interval of F_8 and compute the excess of the average spectrum. Consider, for instance the arithmetic average of the spectra of the subgroup with $2 < F_8 \leq 7.5\,10^{-14}\,\mathrm{Wm}^{-2}\,\mu\mathrm{m}^{-1}$: this group of 15 objects contains no obviously spurious spectrum, and the average spectrum is quite smooth. This spectrum can be modeled using a spherical radiative transfer model (see Sect. 5), and $\bar{\mathscr{E}}_{10}$ is then deduced from the model spectrum. This procedure reduces the relative weight of the most noise-ridden fluxes ($\lambda \sim 8\,\mu$m) in the determination of $\bar{\mathscr{E}}_{10}$; it leads to the conservative estimate $\bar{\mathscr{E}}_{10} \geq 7.5$ (below this value, the model spectrum is unacceptably distorted even at $\lambda > 8\,\mu$m). This lower bound is not directly comparable with the averages in Fig. 6 because the excess of the average spectrum is always smaller than the average excess. This results from the facts that a) noise affects a variable ($F_8 \equiv F_{\lambda_0}$) which occurs in the denominator of Eq. (5) so that large excesses are favored in averaging the excesses and b) in averaging spectra, we normalize at the peak ($\lambda = 10\,\mu$m) so that intrinsically smaller excesses are favored in this process, even in absence of noise.

Thus, for the extreme subgroup considered here, the true average excess (in the sense of Fig. 6a) lies certainly above 7.5. Taking into account the intrinsic dispersion of excesses, it may safely be concluded that the tail of the distribution comprises still larger true excesses, although the highest dots to the left of Fig. 5 are artefacts due to noise. Still more interesting is the anticorrelation of $\bar{\mathscr{E}}_{10}$ with F_8; since F_8 is naturally anti-correlated with galactic distance, this points to an increase of average excess towards the galactic bulge. We shall return to the subject of galactic distribution in Sect. 4.

A final information can be gathered from Fig. 7, which represents the correlation between the excess at 10 μm ($\mathscr{E}_{10}$) and the colour F_{14}/F_8, the ratio of flux densities around 14.5 and 8 μm. The latter is sensitive to the star continuum slope. A rough estimate can be made of the range of star colour temperatures, T_*, involved. First, we note that no obvious correlation was found between envelope colour and luminosity. We are therefore allowed to adopt, as a common "effective" envelope temperature, the average value for all the objects of interest, i.e. $\sim$ 300 K (from Fig. 3). Then, using the same simple model as above, we construct a set of curves $F_{14}/F_8 = f(\mathscr{E}_{10})$, each for a given star colour temperature. Superposing this network upon Fig. 7, we observe that the vast majority of data points spans the range of T_* from 700 K to $\sim$5000 K. The curve for $T_* = 2500$ runs through the densest regions of the cloud of points over the whole range of $\mathscr{E}_{10}$'s.

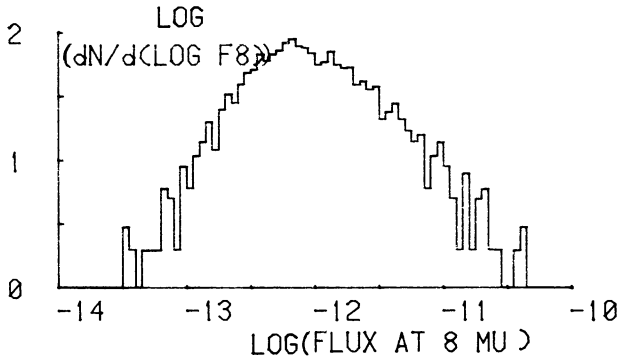

Fig. 6b. A histogram of class 2 in equal intervals of $\log F_8[\Delta(\log F_8) = 0.05]$. F_8 in $\mathrm{Wm}^{-2}\,\mu\mathrm{m}^{-1}$

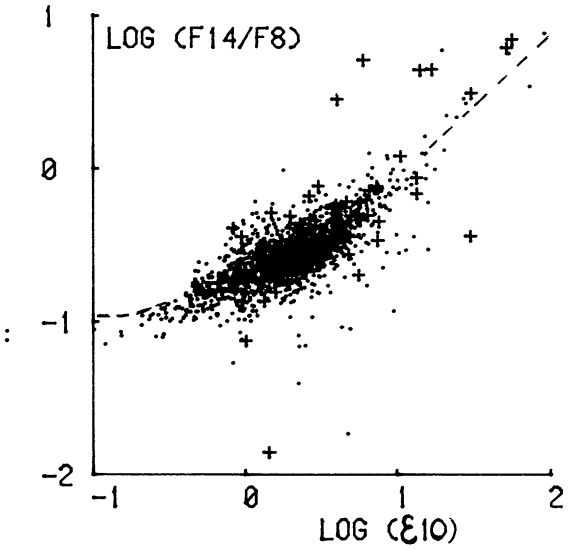

Fig. 7. The color F_{14}/F_8 as a function of the 10-μm relative excess. This leads to an estimate of the range of photospheric temperatures involved (see text). Dots for class 2, crosses for class 6; 1808 objects in all. Dashed line: model for $T_* = 2500$ K

From Figs. 1, 3, 4, 5 and 7, it appears that the objects of class 6 do not differ qualitatively from those of class 2. They can be considered as forming a subclass of class 2, only with extreme characteristics: lower star colour temperatures, larger excesses, fainter (more distant) objects and broader silicate features, in general.

4. The galactic distribution of envelopes

Because of its large size, the silicate-dust set of objects lends itself to a study of galactic distribution. A plot of b^{II} against l^{II} for all of the 2008 objects clearly shows at least 2 populations: one is quasiisotropic and likely to comprise the neighbouring red giants; the other crowds near the galactic plane and is particularly dense in the range $-90° \leq l^{\mathrm{II}} \leq 90°$, indicating that the survey reaches at least as far as the inner arms. To be more quantitative, we have to restrict the ranges of l^{II}, b^{II} and F_8 (the flux density at 8 μm), for instance. Figure 8 shows a histogram, in bins of 5° in l^{II}, of the sub-class defined by $|b^{\mathrm{II}}| \leq 2.5°$ and $F_8 < 5\,10^{-13}\,\mathrm{Wm}^{-2}\,\mu\mathrm{m}^{-1}$ ($\sim$11 Jy). This is reminiscent of the grand design of the Galaxy, with the nuclear bulge and inner arms as suggested by radio, optical and near IR data (Scoville, 1975; Elmegreen, 1985; Okuda, 1983). This structure is gradually blurred by closer objects as the limiting $|b^{\mathrm{II}}|$ and F_8 increase. It is also probably dis-

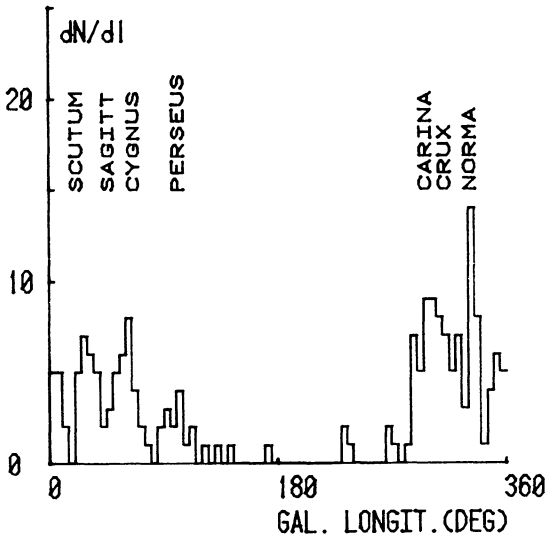

Fig. 8. Galactic distribution, in longitude, of the 189 faintest objects of class 2*n* and 6*n*, within 2°5 from the galactic plane. The approximate locations of the galactic arms are indicated in the upper part of the figure. Bins of 5°

torted by the incompleteness of the IRAS survey at the level $F_{12} \sim 10$ Jy (Beichman et al., p. IX-21) and by the deliberate exclusion of sources subject to confusion, especially within 10° of the galactic center (gc) (ibid, P.I-2).

The fact that the "arms" structure is blurred for $F_8 \gtrsim 11$ Jy should be related to the distribution of the 10-μm excess as a function of F_8 (Fig. 6a). All this together may be telling us that we are in the presence of two sub-classes of objects, one which is relatively close to the Sun and dominated by red giants, and another, reaching to the g.c., which is dominated by red supergiants, since only supergiants ($M_V < -7$) can be seen at such large distances. Hence, we infer that supergiants with large excesses and luminous envelopes tend to occur in the inner Galaxy; those which are close to the galactic plane fall preferentially near the galactic arms.

Now, if we consider the 39 objects with $\mathscr{E}_{10} > 10$, in classes 2 and 6, practically all of them are found to lie in the direction of the bulge and only about one third are located near the galactic plane ($|b^{II}| \leq 2.5°$). This should be related to the bulge population of evolved, late type M stars found by Habing et al. (1985) in the IRAS point source Catalog. It should be recalled that the supergiant population of the bulge is dominated by a supermetal rich component (Whitford, 1985).

Let us now consider the distribution of bright (nearby) objects. Figure 9 represents the histograms of objects with $F_8 \geq 3\,10^{-12}\,\mathrm{Wm^{-2}\,\mu m^{-1}}$ (~ 66 Jy) and relative excesses at 10 μm, $\mathscr{E}_{10}$, respectively ≤ 1 (full line) and > 2 (dashed line). It is clear that the larger excesses are confined to smaller galactic latitude. More quantitatively, subdivide the group of objects with $F_8 \geq 22$ Jy into subclasses defined by different, contiguous intervals in which the relative excess, $\mathscr{E}_{10}$, may fall: 0–1, 1–2, 2–3, 3–4, 4–5; then construct a histogram in b^{II} for each subclass, and compute the corresponding standard deviation of b^{II} from its mean, $\sigma_{b^{II}}$. This is found to decrease rather steadily as $\mathscr{E}_{10}$ increases: 24, 18.5, 18, 14, and 8°, respectively. This is still another similarity between the 10-μm excess and the metallicity distributions in the Galaxy, inasmuch as galactic latitudes are correlated with heights above the galactic plane. This, in turn, is likely to be the case for the relatively small range of F_8 considered here, if the latter is proportional to the luminosity of the photosphere, as explicitely assumed in the definition of the IR excess. This assumption is justified by model computations of F_8/F_* (8 μm) for the range of excesses considered here and using our optical properties for silicate: $Q_{abs}/a = 0.08$ and 1.12 for $\lambda = 8$ and 10 μm, respectively.

Another exciting possibility would be that large excesses are correlated with large mass losses and (hence) star masses.

5. Radiative modeling

A more sophisticated radiative modeling than the one used above, can help to extract more accurate values of the photosphere and envelope parameters. Consider, for instance, the average spectrum of class 6 (Fig. 1), on the assumption that this truly represents the characteristics of individuals in that class, notwithstanding the effects of noise. As in Sect. 3, we use the dust emitting properties deduced by Pégourié and Papoular (1985) and Pégourié (1985) from ground-based spectra of oxygen-rich stars. To make sure that these are valid for the IRAS spectra too, we first modeled the average spectrum of class 2c (Fig. 1; bright spectra, neighbouring objects), using a spherical radiative model derived by Pégourié (1985) from Lefèvre et al. (1982), with a dust envelope of optical thickness τ (at 10 μm), inner temperature T_d and a density distribution in r^{-2}, starting from its inner boundary r_1 and centered around a star of radius r_* and star colour temperature T_*. The optimum model is obtained for $T_* = 3500$ K, $\bar{a} = 1.6\,\mu$m, $\tau(r_1/r_*)^2 = 29$ and $T_d(r_1) = 450$ K, and the corresponding spectrum is shown in Fig. 9, together with the average of class 2c. The discrepancy in the range 13–16 μm ($\sim 15\%$) was not unexpected since the corresponding dust properties are very poorly determined by ground-based observations, due to telluric absorption. The fit is otherwise acceptable.

Now, turning to the average spectrum of class 6, it was only possible to fit it with a model using a radial density distribution

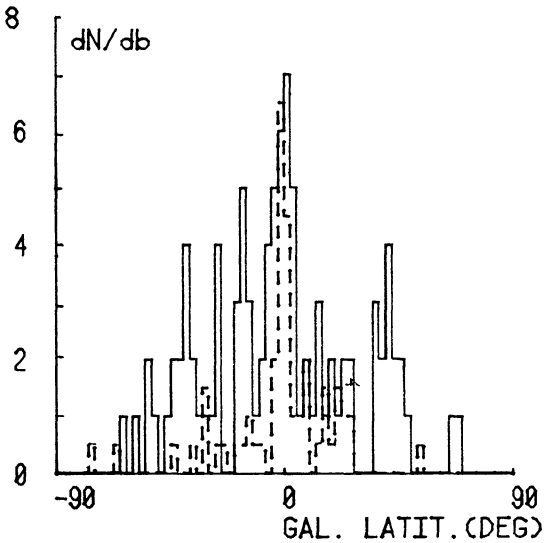

Fig. 9. Histograms in galactic latitude of the brightest objects ($F_8 \geq 66$ Jy, or $3\,10^{-12}\,\mathrm{Wm^{-2}\,\mu m^{-1}}$) of classes 2*n* and 6*n*. Full line: relative excess at 10 μm, $\mathscr{E}_{10} \leq 1$ (95 objects); dashed line: $\mathscr{E}_{10} \geq 2$ (62 objects; scale halved). Bins of 2°5

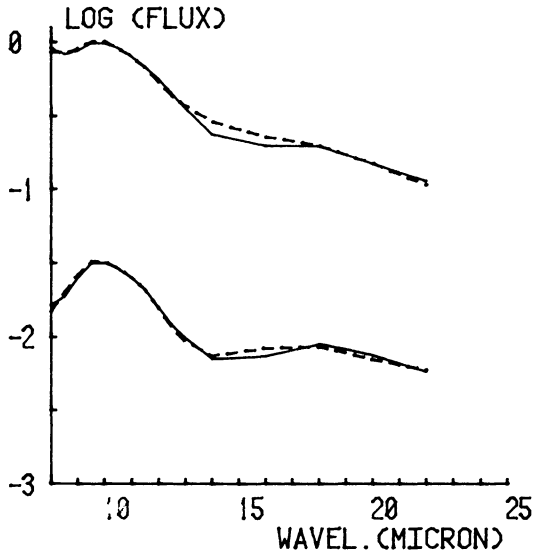

Fig. 10. Average LRS spectra (dashed lines) and their radiative-transfer models (full lines) for classes 2c (above) and 6 (lowered by 1.5 ordinate units); cf. Fig. 1. See Sect. 5 for the parameters of the models

in $r^{-0.9}$ and including 50% of amorphous $MgSiO_3$ in the dust (Papoular and Pégourié, 1983). The other parameters of the model are $T_* = 1000\,K$, $T_d(r_1) = 550\,K$, $\bar{a} = 1.5\,\mu m$ and $\tau(r_1/r_*)^2 \simeq 3.4$; the corresponding spectrum is shown in Fig. 10, together with the average of class 6.

Here also, the agreement is satisfactory. The low colour temperature suggests that part of the continuum is due to free-free or free-bound radiation; for, if the photosphere was as cool as 1000 K, then r_1/r_* would be of order 1 (Papoular and Pégourié, 1986) so that τ would be larger than 1, which is incompatible with the discussion of Figs. 4 and 7. On the other hand, some supergiants with relatively high photospheric temperatures and ratio r_1/r_* are known to have intermediate, ionized envelopes whose continuum emission is indeed characterized by low colour temperatures: HR5171, V915 Sco for instance (Pégourié and Papoular, 1985).

Acknowledgements. It is a pleasure to acknowledge the friendly and generous help of N. Pétrou, J. Jorrand and P. Masse (Service d'Astrophysique, Saclay) with the computer work. Thanks are also due to F. Olnon for essential information on noise and selection in the LRS data.

Appendix

The interest in a possible anti-correlation between $\mathscr{E}_{10}$ and F_8 warrants the use of some algebra to justify the interpretation of Fig. 5 that is given in the main text.

A1. Diffusion

Consider first the apparent increase of the $\mathscr{E}_{10}$ due to the spreading (diffusion) of points along lines of constant $(\mathscr{E}_{10} + 1)\,F_8$, because of noise and in absence of truncation. Assume a normal (Gaussian) distribution of the noise affecting F_8, i.e. the probability density of measuring a value $F\,(\equiv F_8)$ at $\lambda = 8\,\mu m$, instead of the true value F_t is

$$p(F, F_t) = [(2\pi)^{1/2}\sigma_F]^{-1} \exp\{-[(F - F_t)/\sigma_F\sqrt{2}]^2\} \tag{A1}$$

where $\sigma_F = 4\,10^{-14}/\sqrt{2}\,Wm^{-2}\,\mu m^{-1}$ (the reason for the factor $1/\sqrt{2}$ is that F_8 is an average over the fluxes at 2 adjacent wavelength's). The erroneous $\mathscr{E}$ corresponding to F is related to the true excess $(\mathscr{E}_t)$ by

$$(\mathscr{E} + 1)F = (\mathscr{E}_t + 1)F_t \tag{A2}$$

Assume also that F_{10} is not affected by noise.

Let there be $\dot{n}_t(F_t)\,dF_t$ objects with true excess $\mathscr{E}_t(F_t)$ in an interval dF_t. What is to be detected in an interval $F, F + dF$ of measured flux? The contribution of dF_t will consist in a number

$$dn = \dot{n}_t(F_t)\,dF_t[p(F, F_t)\,dF]$$

of objects with $\mathscr{E}$ satisfying (A2). Then, the new (observed) average excess will be

$$\bar{\mathscr{E}}_0 = \int_{F_t} \mathscr{E}\,dn \Big/ \int_{F_t} dn = \frac{\int (\mathscr{E}_t + 1)F_t/F\dot{n}_t p(F, F_t)\,dF_t}{\int \dot{n}_t p(F, F_t)\,dF_t} - 1 \tag{A3}$$

and the population density will become

$$\dot{n}_0 = \int_{F_t} \dot{n}_t p(F, F_t)\,dF_t \tag{A4}$$

The changes in $\bar{\mathscr{E}}_0$ and $\dot{n}_0$ increase with σ_F, $|d\mathscr{E}_t/dF_t|$ and $|d\dot{n}_t/dF_t|$ and vary with F. This is illustrated in Fig. (A1) for a distribution of $\mathscr{E}_t$ (dotted line) that roughly approximates $\bar{\mathscr{E}}_{10}$ of Fig. 6a near $F_8 = 10^{-13}$, and a distribution of $\dot{n}_t$ (full line) that roughly approximates the histogram of Fig. 6b in the same range of F_8:

$$\mathscr{E}_t = 5(F_t/10^{-13})^{-1/3}, \qquad \dot{n}_t = 8\,10^{14}(F_t/10^{-13})^{1.5}.$$

In this case, the effect of $d\dot{n}_t/dF_t$ is dominant and is quite large for $F \gtrsim 10^{-13}$. However, beyond $2\,10^{13}$, it is negligible ($\bar{\mathscr{E}}_0/\mathscr{E}_t$ and $\dot{n}_0/\dot{n}_t \to 1$); this is also true for a distribution of $\mathscr{E}$'s.

A2. Selection

We now turn to the effects of noise in the presence of selection, and assume a common $\mathscr{E}_t$-distribution and a unique $\dot{n}_t$ for all F_8's. This allows us to study the alterations of the intrinsic distribution in each finite F_8-interval, ΔF, of Fig. 6a, without consideration to the previous "diffusion" effects.

A study of the histograms of observed $\bar{\mathscr{E}}$'s for the (noiseless) subgroups with $F_8 > 10^{-12}$ points to a Poissonian distribution for the $\mathscr{E}_t$'s:

$$p_t(\mathscr{E}_t) = \frac{\lambda^k e^{-\lambda}}{k!} \tag{A5}$$

where $\lambda \equiv (\bar{\mathscr{E}}_t/\sigma_t)^2$ and $k \equiv \lambda\mathscr{E}_t/\bar{\mathscr{E}}_t$.

For any one value of F_t in ΔF, a given $\mathscr{E}_t$ will transform into $\mathscr{E}$, according to (A2), if F_t is changed into F. The probability for this event is

$$p_n(\mathscr{E}, \mathscr{E}_t) = -p_F(F, F_t)F_t(\mathscr{E}_t + 1)/(\mathscr{E} + 1)^2. \tag{A6}$$

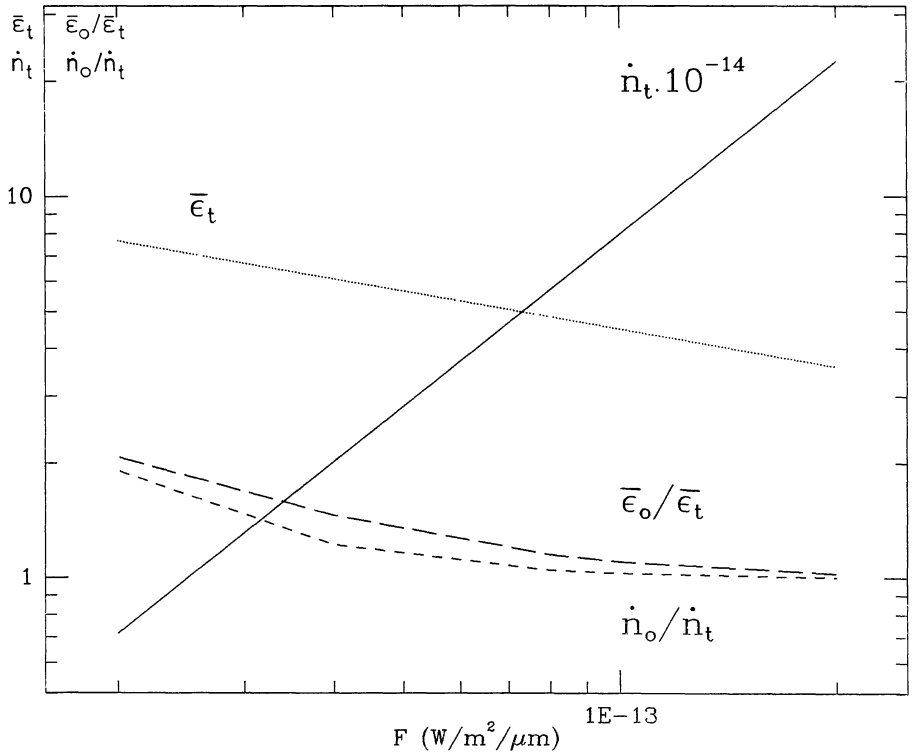

Fig. A1. The "diffusion" effect of noise on the distribution of apparent average excesses, $\bar{\mathscr{E}}_{10}\dot{n}_t$ (——) and $\mathscr{E}_t$ (. . . .): assumed density and excess at given F_8; $\dot{n}_0$ and $\bar{\mathscr{E}}_0$: apparent density and average excess associated with noise on F_8; the extent of the perturbation is described by $\dot{n}_0/\dot{n}_t$ (small dashes) and $\bar{\mathscr{E}}_0/\mathscr{E}_t$ (long dashes)

The observed value of F should be restricted to ΔF, but it can also be restricted by truncation if the corresponding $\mathscr{E}$ is lower than $10\sigma_F/F$.

Thus, given $\bar{\mathscr{E}}_t$ and σ_t, it is possible, using Eqs. (A1, 5 and 6), to derive the parameters *expected* to be observed: the average excess, $\bar{\mathscr{E}}_{10}$ and the standard deviation of excesses $\sigma_{\mathscr{E}}$. Figure A2 illustrates the case where the values $\bar{\mathscr{E}}_{10} = 1.6$, $\sigma_{\mathscr{E}} = 1$, observed at the largest fluxes, are adopted as intrinsic parameters for the whole range of F_8. Distorsions of the distribution appear at $\sim 3\,10^{-13}$ and quickly increase as F_8 decreases. For larger $\bar{\mathscr{E}}_t$'s and the same σ_t, distortions set in for lower F_8's.

Figure A2 also shows that a uniform distribution of $\mathscr{E}_t$'s, independent of F_8 and identical with the distribution observed at large fluxes cannot give rise to the observed distributions of $\bar{\mathscr{E}}_{10}$ and $\sigma_{\mathscr{E}}$ (Fig. 6a). Note, in particular, the distinct and characteristic dip in $\sigma_{\mathscr{E}}$, near $F_8 = 10^{-13}$, in Fig. A2.

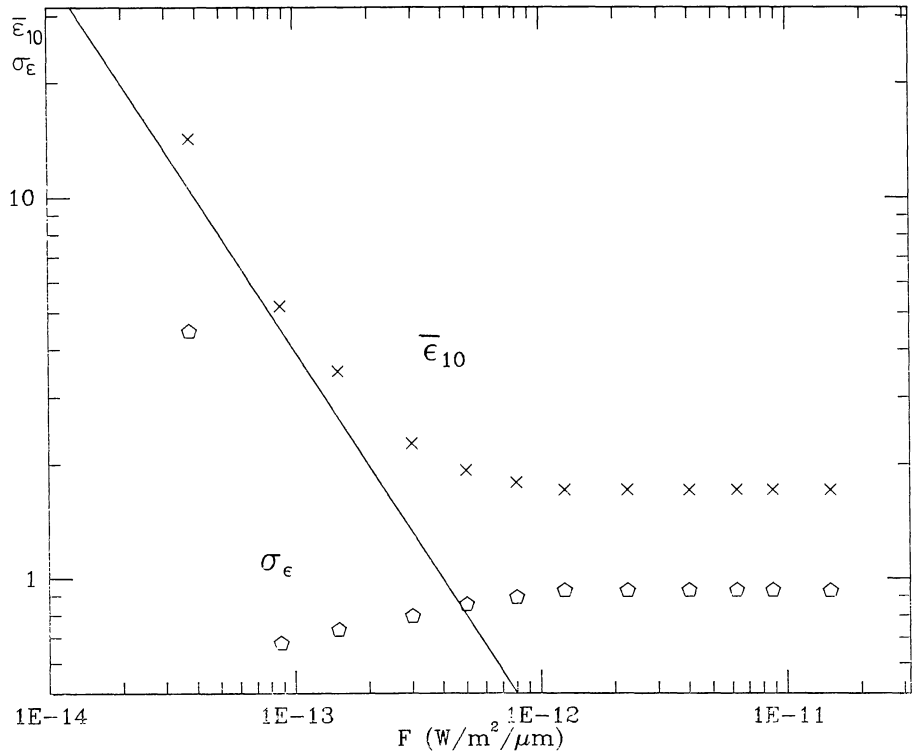

Fig. A2. The effect of selection in the presence of noise on F_8. Assumed underlying (intrinsic) distribution: $\bar{\mathscr{E}}_t = 1.6$, $\sigma_t = 1$ (cf. Fig. 6a for large F_8's). $\bar{\mathscr{E}}_{10}$ (crosses) and $\sigma_{\mathscr{E}}$ (pentagons) are the modifications of $\bar{\mathscr{E}}_t$, σ_t expected to result from the selection algorithm (oblique line)

A3. Inverse problem

Having acquired a feeling of the different effects involved, we can now use Sect. A2 to estimate the two parameters of the parent distribution, by tailoring them so that the derived parameters expected to be observed are as close as possible to the *effectively* observed parameters. This was done for each subgroup of Fig. 6a, with the following result:

a) for $F_8 \gtrsim 10^{-12}\,\mathrm{Wm}^{-2}\,\mu\mathrm{m}^{-1}$, the only possible choice for $\bar{\mathscr{E}}_t$, σ_t was the corresponding observed pair $\bar{\mathscr{E}}_{10}$, $\sigma_{\mathscr{E}}$ (no noticeable truncation by selection);

b) for $1.5\,10^{-13} \gtrsim F_8 \gtrsim 10^{-12}$, of the possible solutions, we chose the pair with minimum $\bar{\mathscr{E}}_t$; $\bar{\mathscr{E}}_t/\bar{\mathscr{E}}_{10}$ is always $\gtrsim 1$ and decreases with F_8 to reach ~ 0.85 for $F_8 = 1.5\,10^{-13}$ (increasing truncation, also indicated by $\sigma_t/\sigma_{\mathscr{E}} > 1$). $\bar{\mathscr{E}}_t$ and σ_t are represented in Fig. 6a by crosses and pentagons;

c) for $F_8 \gtrsim 1.5\,10^{-13}$, it is no longer possible to find a suitable pair $\bar{\mathscr{E}}_t$, σ_t; this is a result of increasing diffusion (cf. Sect. A2), which is not taken into account in the present procedure.

References

Beichman, C.A., Neugebauer, G., Habing, H.J., Clegg, P.E., Chester, T.J. (eds.): 1985, *IRAS Explanatory Suppl.*, JPL, Pasadena

Elmegreen, D.M.: 1985, in *The Milky Way Galaxy*, H.V. Woerden et al. (eds.), Reidel, p. 255

Forrest, W.J., Gillett, F.C., Stein, W.A.: 1975, *Astrophys. J.* **195**, 423

Forrest, W.J., McCarthy, J.F., Houck, J.R.: 1979, *Astrophys. J.* **233**, 611

Gillett, F.C., Forrest, W.J., Merrill, K.M., Capps, R.W., Soifer, B.T.: 1975, *Astrophys. J.* **200**, 609

Habing, H.J., Olnon, F.M., Chester, T., Gillett, R., Rowan-Robinson, Neugebauer, G.: 1985, *Astron. Astrophys.* **152**, L1

Lefèvre, J., Bergeat, J., Daniel, J.Y.: 1982, *Astron. Astrophys.* **114**, 341

Okuda, H.: 1983, in *The Milky Way, IAU Symp.* **106**, H.V. Woerden, R.J. Allen, W. Butler Burton (eds.), Reidel

Olnon, F.M.: 1985, 1st. IRAS Symposium *Light on Dark Matter*, Noordwijk, p. 31

Papoular, R., Pégourié, B.: 1983, *Astron. Astrophys.* **128**, 355

Pégourié, B., Papoular, R., 1985, *Astron. Astrophys.* **142**, 451

Pégourié, B., 1985, Thèse (Univ. Paris VII)

Papoular, R. and Pégourié, B., 1986, *Astron. Astrophys.* **156**, 199

Scoville, N.Z., 1975, *Astrophys. J. Letters*, **199**, L105

Whitford, A.E., 1985, *Publ. Astron. Soc. Papers*, **97**, 205

Wildeman, K.J., Beintema, D.A., Wesselius, P.R., 1983, *J. British Interplanet. Soc.*, **36**, 21